PHYSICAL REVIEW E **73**, 036704 (2006)

Computation of uniform wave forms using complex rays

Dario Amodei*
Department of Physics, Stanford University, Stanford, California, 94305 USA

Henk Keers
Schlumberger Cambridge Research, Madingley Road, Cambridge, CB3 0EL, United Kingdom

Don Vasco and Lane Johnson
Lawrence Berkeley National Laboratory, 1 Cyclotron Road, Berkeley, California, 94720 USA

(Received 25 October 2005; published 8 March 2006)

Complex rays and polynomial phase functions are used to numerically solve the Helmholtz equation in a realistic two-dimensional smoothly varying heterogeneous velocity model with multiple adjacent cusp caustics. Together these two methods allow the determination of global uniformly asymptotic solutions in the presence of arbitrarily many caustics. Two algorithms are introduced to this end: a two-point ray tracing algorithm for complex rays and a perturbation method for constructing polynomial phase functions. Model representation in complex space is performed via discrete cosine transform analysis. Geometrical and uniformly asymptotic solutions are computed for a linear layer test model as well as a velocity model from Yucca Mountain.

DOI: 10.1103/PhysRevE.73.036704 PACS number(s): 42.15.Dp, 03.65.Sq, 43.20.+g, 91.30.−f

I. INTRODUCTION

Asymptotic methods are often the tool of choice for modelling the propagation of waves through heterogeneous media. Their advantages are numerous: They are faster and more physically intuitive than fully numerical techniques such as finite differences (FD), while also being specifically valid at high frequencies. In large three-dimensional (3D) models where fully numerical techniques are computationally very expensive, asymptotic methods may be the only available techniques. Applications of asymptotic methods in wave propagation include acoustics [1,2], electrodynamics [3–5], seismology [6,7], semiclassical mechanics [8,9], and gravitation [10].

Unfortunately, asymptotic methods encounter the problem of caustics. The simplest asymptotic method, zeroth-order asymptotic ray tracing, (ZART), produces nonphysical wavefield singularities at caustics. A number of theoretical techniques have been developed to circumvent this problem, including Maslov theory [11], Gaussian beams [12,13], coherent state approximations [14], and direct use of the caustic classification theorem [15,16]. Numerically, however, each of these methods has its problems, especially in two and three dimensions. The Maslov integral solution to the caustic problem consists of a series of overlapping local solutions that must be computed and patched together with partitions of unity. If this is not done carefully then it could give rise to numerical problems, including pseudocaustics [17,18]. Gaussian beams and coherent states both contain a nonunique parameter. Finally, direct use of the classification theorem applies only to one caustic at a time, requiring local solutions to be combined as in Maslov theory.

A theoretical alternative has been proposed by Ludwig [19] using the method of polynomial phase functions. There are however two practical obstacles to this approach. The first is that to be continuous in caustic shadows this method requires the use of complex rays (or alternatively the higher-order extrapolation of phase functions into the shadow region [20]). The second is the computation of the polynomial phase functions.

In this paper we present numerical algorithms that remove both obstacles. Our complex ray algorithm builds on a large body of work. Complex rays have been used in optics for over 40 years; the earliest references known to the authors are Seckler and Keller [21] and Budden [3]. More recent theory can be found in [22–24]. Egorchenkov and Kravtsov [25] presented what appears to be the first numerical realization of complex ray tracing in smoothly varying inhomogeneous media. Their implementation was limited to the case of a 1D stratified medium. Another recent implementation focused on the relation between complex rays and Gaussian beams [26]. Our focus will be the tracing of complex rays in general 2D smooth inhomogeneous media, though most of the theory is also valid in 3D. Our computational algorithm for polynomial phase functions builds on the work of Connor and Curtis [27] and Connor *et al.* [28,29].

The next section (Sec. II) is devoted to the basic ideas of ray tracing and uniform asymptotics. We will then provide a brief summary of the theory of complex rays in Sec. III, followed by a new numerical method for the computation of complex rays (Sec. IV). After considering issues of model representation (Sec. V) and testing our methods on some specific velocity models (Sec. VI), we will return to the equations derived in Sec. II [for future reference these are Eqs. (14)–(18)] and present an algorithm for their solution in the general complex case (Sec. VII). Finally, in Sec. VIII we will use the solutions of these equations to calculate uniform time-domain waveforms, which we will compare with wave forms from geometric ray tracing in both the real and complex cases.

---

*Electronic address: damodei@stanford.edu

1539-3755/2006/73(3)/036704(14)/$23.00

II. RAY TRACING AND UNIFORM ASYMPTOTICS

Consider the Helmholtz equation

$$\Delta \hat{u}(\mathbf{x},\omega) + \frac{\omega^2}{c(\mathbf{x})^2}\hat{u}(\mathbf{x},\omega) = 0. \tag{1}$$

Here c denotes the real-valued velocity, ω is the frequency, and $\hat{u}$ is the unknown pressure field in the frequency domain. The position vector is denoted by $\mathbf{x}$. We seek high frequency ($\omega \to \infty$) solutions of Eq. (1), and therefore substitute the distorted plane wave solution

$$\hat{u}(\mathbf{x},\omega) = A(\mathbf{x})\exp[i\omega T(\mathbf{x})] + \mathrm{O}(\omega^{-1}), \tag{2}$$

in Eq. (1). Equation (2) represents a ray with travel time $T(\mathbf{x})$ and amplitude $A(\mathbf{x})$ [4,6,7,16]. Taking highest orders in ω gives the eikonal equation

$$(\nabla T)^2 = c^{-2}, \tag{3}$$

and the transport equation

$$2\,\nabla A \cdot \nabla T + A \Delta T = 0. \tag{4}$$

Equation (3) can be solved by taking its bicharacteristics (rays), namely,

$$\frac{d\mathbf{x}}{d\nu} = \mathbf{p} \tag{5}$$

$$\frac{d\mathbf{p}}{d\nu} = -\frac{1}{2}\nabla c^{-2}(\mathbf{x}), \tag{6}$$

where $\mathbf{p} = \nabla T$ and ν is the ray parameter. Equation (4) can be solved by taking the derivatives of Eqs. (5) and (6) with respect to the initial take-off angle (together with the appropriate initial conditions). Numerical techniques to solve the Hamiltonian system given by Eqs. (5) and (6) are completely standard if c is real and smooth (e.g., [30]). In the case of multiple arrivals, Eq. (2) becomes

$$\hat{u}(\mathbf{x},\omega) = \sum_{n=1}^{N} A_n(\mathbf{x})\exp[i\omega T_n(\mathbf{x})] + \mathrm{O}(\omega^{-1}). \tag{7}$$

Unfortunately, this Ansatz breaks down near caustics. The amplitude A becomes unphysical near caustics and infinite on caustics. We would like to replace Eq. (7) with an expression that asymptotically solves the Helmholtz equation throughout the model space, including at caustics (such an expression is called uniformly asymptotic). It has been shown [15,16,19,31] that for a generic medium $c(\mathbf{x})$ there always exist uniformly asymptotic solutions of the form

$$\hat{u}(\mathbf{x},\omega) = (\omega/2\pi i)^{m/2}\int_{\mathbb{R}^m} a(\mathbf{x},\theta)\exp[i\omega\Phi(\mathbf{x},\theta)]d\theta^m + \mathrm{O}(\omega^{-1}). \tag{8}$$

To understand which expressions of the form (8) are uniformly asymptotic solutions, it is necessary to examine the ω dependence of these integrals. For each $\mathbf{x}$, let $\{\theta_k(\mathbf{x})\}_{k=1}^{K}$ be the set of θ for which

$$\frac{\partial \Phi}{\partial \theta}(\mathbf{x},\theta) = \mathbf{0}. \tag{9}$$

Application of the principle of stationary phase [11,15] then yields

$$\hat{u}(\mathbf{x},\omega) = \sum_{k=1}^{K}\left\{ a(\mathbf{x},\theta_k(\mathbf{x}))\exp[i\omega\Phi(\mathbf{x},\theta_k(\mathbf{x}))] \times \left(\det \left.\frac{\partial^2\Phi}{\partial\theta^2}\right|_{\theta_k(\mathbf{x})}\right)^{-1/2}\right\} + \mathrm{O}(\omega^{-1}), \tag{10}$$

provided that $\det \partial^2\Phi/\partial\theta^2|_{\theta_k(\mathbf{x})} \neq 0$ (the branch of the square root is chosen so that $1^{1/2}=1$, and a branch cut is made below the negative real axis). Comparison of Eq. (10) with Eq. (7) when both are valid yields the requirements

$$K = N \tag{11}$$

$$\Phi(\mathbf{x},\theta_n(\mathbf{x})) = T_n(\mathbf{x}) \tag{12}$$

$$a(\mathbf{x},\theta_n(\mathbf{x})) = \left(\det \left.\frac{\partial^2\Phi}{\partial\theta^2}\right|_{\theta_n(\mathbf{x})}\right)^{1/2} A_n(\mathbf{x}), \tag{13}$$

for $n=1,\ldots,N$, with a suitable relabeling of indices. These equations can be found in Refs. [19,32–34].

In fact, it can be shown that any well-behaved integral representation of the form (8), such that Eqs. (11)–(13) hold, is a uniformly asymptotic solution of the Helmholtz equation [15,16]. Therefore, considerable freedom exists in choosing the functions a and Φ. Typically the functions are supplied by methods such as Maslov theory, coherent states, or Gaussian beams; we will instead use Eqs. (11)–(13) more directly. In particular, we will obtain a unique solution to these equations by requiring a and Φ to be polynomials in θ.

We will restrict our attention to one-dimensional integrals, i.e., $m=1$ in Eq. (8). In practice this is only moderately restrictive: A uniformly asymptotic integral with $m=1$ exists in all 2D model spaces and in those 3D model spaces not containing a hyperbolic or elliptic umbilic caustic [35].

In the case of a one-dimensional integral, the relevant conditions for Φ are

$$\Phi(\mathbf{x},\theta_n(\mathbf{x})) = T_n(\mathbf{x}) \tag{14}$$

$$\left.\frac{\partial\Phi}{\partial\theta}\right|_{\theta_n} = 0, \tag{15}$$

and for a simply

$$a(\mathbf{x},\theta_n(\mathbf{x})) = \left(\left.\frac{\partial^2\Phi}{\partial\theta^2}\right|_{\theta_n(\mathbf{x})}\right)^{1/2} A_n(\mathbf{x}). \tag{16}$$

To avoid under- or over-determination, we fix the order of the polynomials as follows:

$$\Phi(\mathbf{x},\theta) = \frac{1}{N+1}\theta^{N+1} + \sum_{n=0}^{N-1} P_n(\mathbf{x})\theta^n \tag{17}$$

$$a(\mathbf{x},\theta) = \sum_{n=0}^{N-1} Q_n(\mathbf{x})\theta^n. \tag{18}$$

Note that the Eqs. (14), (15), and (17) for Φ are nonlinear since they require the determination of the θ_n's and P_n's, while the Eqs. (16) and (18) for a are linear once Φ and the θ_n's have been determined.

Unfortunately, the value of N $(=K)$ changes abruptly as a caustic is crossed, so the functions P_n and Q_n may not be continuous at caustics. The expression (8) may therefore fail to be uniformly asymptotic at caustics, defeating the purpose of the integral representation. In particular, Eq. (8) blows up in the shadow zone of any caustic other than the simple fold. Consider, for example, a ray passing through a cusp caustic point in two dimensions. In the lit region there are three arrivals and Eq. (8) forms a Pearcey integral, which remains finite as the cusp is approached. In the shadow zone, however, there is only one arrival, so the phase function Φ is a simple quadratic. As the caustic is approached, the geometric amplitude $A_1(\mathbf{x})$ tends to infinity, and Eq. (16) shows that $a(\mathbf{x},\theta)$ also tends to infinity, for all values of θ. It is then easy to see that Eq. (8) increases without bound as the cusp is approached. Thus the "uniform" expression (8) is both discontinuous and divergent at the cusp. For rays that pass near the cusp without touching it, Eq. (8) is no longer divergent, but remains discontinuous and therefore nonuniform. What is needed is a constant number of geometric arrivals at all points in space, so that N does not vary. To gain such uniform coverage, it is necessary to include complex rays.

III. COMPLEX RAYS: THEORY

This section contains a brief overview of complex kinematic and dynamic ray tracing, in preparation of the two point complex ray tracing presented in the next section. General background can also be found in [22–24]. Chapman *et al.* [24] also provides a detailed exploration of selection rules.

In order to obtain the exponentially decaying solutions in caustic shadows, it is necessary to complexify all aspects of the ray tracing. Consider again Hamilton's equations in n dimensions

$$\frac{d\mathbf{x}}{d\nu} = \mathbf{p},$$

$$\frac{d\mathbf{p}}{d\nu} = -\frac{1}{2}\nabla c^{-2}(\mathbf{x}), \tag{19}$$

but now let ν, $\mathbf{x}$, $\mathbf{p}$, and c be complex (c is still assumed real for real $\mathbf{x}$). The rays thus travel in a position space $\mathbf{x}$ of $2n$ real dimensions and phase space $(\mathbf{x},\mathbf{p})$ of $4n$ real dimensions. c must be extended to an analytic function of n complex variables. The most significant change, however, comes from the complexification of ν.

A complex ν implies that Hamilton's equations no longer trace out uniquely defined paths in phase or position space. Given an initial value $(\mathbf{x}_0,\mathbf{p}_0)$, Eqs. (19) may be integrated along an arbitrary curve in the complex ν plane. Integrating along the curves $\arg \nu=\text{constant}$ produces infinitely many nonintersecting paths emanating from the same point in phase space. In fact, if there is one path joining any two points in phase space, there are necessarily infinitely many paths joining them, because the curve of integration can always be perturbed in the ν plane. To resolve this seeming nonuniqueness, a complex ray is defined as the two-dimensional surface parametrized by

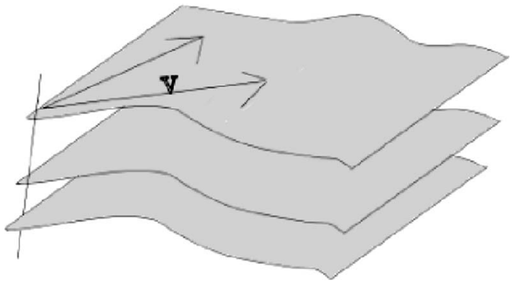

FIG. 1. Schematic diagram of complex ray propagation. Each 2D surface shown is a complex ray. The complex number ν indexes position within a ray. Each ray intersects the surface of initial conditions (transverse line) at exactly one point. Only a one-dimensional projection of the two-dimensional surface of initial conditions is shown.

$$\mathbf{x}(\nu) = \mathbf{x}_0 + \int_{C_0^\nu} \frac{d\mathbf{x}}{d\nu} d\nu,$$

$$\mathbf{p}(\nu) = \mathbf{p}_0 + \int_{C_0^\nu} \frac{d\mathbf{p}}{d\nu} d\nu, \tag{20}$$

over all $\nu \in \mathbb{C}$ and all contours C_0^ν from 0 to ν [22]. The term "path" will be used for a particular contour in the ν plane, to distinguish it from a ray, which refers to the two-dimensional manifold formed by the image of all contours in the ν plane. This distinction is shown graphically in Fig. 1, which displays a family of planar rays along with some intra-ray paths. From a more mathematical perspective, these planar rays are analytic "lines" on a complex Lagrangian manifold; the initial condition surface is the corresponding Cauchy surface. These issues are also discussed in Thomson [22].

If there are singularities of c^{-2}, or its derivatives, or of $\mathbf{x}$ or $\mathbf{p}$, then the ray becomes a Riemann surface; $\mathbf{x}$ and $\mathbf{p}$ will be multivalued. This occurs, for instance, at the interfaces between different media. For the rest of this paper, however, we will assume that there are no interfaces, that c^{-2} is smooth, and that singularities of $\mathbf{x}$ and $\mathbf{p}$ can be avoided. Hanyga and Helle [36] handle the complementary case of a piecewise constant model with interfaces.

Under this assumption, $\mathbf{x}(\nu)$ and $\mathbf{p}(\nu)$ are well-defined single-valued functions, since integration is path independent. This allows the unambiguous determination of most quantities of motion along a given ray. For example, travel time and ray spreading are simply

$$T(\nu,\theta_0) = T_0(\theta_0) + \int_0^{\nu} c^{-2}(\mathbf{x}(\nu))d\nu \tag{21}$$

and

$$J(\nu,\theta_0) = \det \left(\frac{\partial \mathbf{x}(\nu)}{\partial \nu} \quad \frac{\partial \mathbf{x}(\nu)}{\partial \theta_0} \right)\Bigg|_{(\nu,\theta_0)}, \tag{22}$$

where θ_0 represents a surface of initial values containing $(n-1)$ complex dimensions (see Fig. 1 and also [11,23]). The ray amplitude A can be calculated up to a sign from the formula

$$A(\nu,\theta_0) = \frac{g(\theta_0)}{J(\nu,\theta_0)^{1/2}}, \tag{23}$$

where $g(\theta_0)$ is a well-defined function independent of ν. The appropriate branch of $J^{1/2}$ must then be determined from selection rules, which will be discussed shortly.

It is useful first to step back and ask what is the physical significance of complex rays. Only points in real position space are physically meaningful, but rays that travel out of real space and then return do make physical contributions. The only difference between such a ray and an ordinary real ray is that in general it has complex T, $\mathbf{p}$, J, and A. The usual ansatz, Eq. (2), applied to such a ray gives an exponentially decaying wave field if $\operatorname{Im} T > 0$ and a growing wave field if $\operatorname{Im} T < 0$. In fact, since complex rays always come in conjugate pairs [by the model symmetry $c^*(\mathbf{x}) = c(\mathbf{x}^*)$], these two types of solutions always occur together. The growing solution is always unphysical; its removal is an instance of Stokes' phenomenon [24]. The decaying solution is often, but not always, the desired wave field in the caustic shadow. Sometimes it may be removed by Stokes' phenomenon if other rays are present. In general the selection rules for determining this are nontrivial; see [24]. However, in a generic smooth model generated by a point source, the decaying solution is almost always physical in the near shadow zone of a caustic. Thus there is an unambiguous rule for selecting exactly one complex ray as we cross a caustic surface.

This caustic-crossing selection rule for complex rays induces a selection rule for amplitude. Considered as a complex function of complex variables ν and θ_0, $J^{1/2}$ has a branch surface at any caustic, where $J=0$. If we specify that $J^{1/2}$ must be continuous when traced around this branch surface through physical complex rays, a unique choice of amplitude continuation results. That is, a branch of $J^{1/2}$ is selected by making a branch cut through the nonphysical ray. This amplitude selection formula is closely related to the KMAH index (named after Keller, Maslov, Arnold, and Hörmander) in the case of real rays [22].

Finally, the relation between complex rays and ordinary real rays should be made clear. A real ray can be viewed as a path within a complex ray on which $\operatorname{Im} \mathbf{x} = 0$. In 2D, the generic complex ray will intersect the real plane only in a point, but the symmetry $c^*(\mathbf{x}) = c(\mathbf{x}^*)$ produces some complex rays whose intersection with $\operatorname{Im} \mathbf{x} = 0$ is one dimensional. A caustic in real space forms the boundary between rays containing a real path ("real rays") and rays that intersect the real plane only in a point ("complex rays"). The two types of rays undergo a confluence at the caustic. For this reason, the rays in the lit region of a caustic are very close in complex initial-slowness space to those in the near shadow zone. Thus it is possible in theory to locate the complex rays from the much more accessible real rays. In the next section we present an algorithm to this end.

IV. COMPLEX RAYS: TWO-POINT RAY TRACING

Numerical tracing along a single complex ray (one-point ray tracing) is very similar to the tracing of a real ray. Suppose $\mathbf{x}(\nu=0)$, $\mathbf{p}(\nu=0)$ are known for a given ray, and that we wish to trace to a point of arbitrary ray parameter, say $\nu = \nu_0$, along the same ray. Any path from 0 to ν_0 in the ν plane is suitable; for convenience choose the straight line $\arg \nu = \arg \nu_0$. Along this line Hamilton's equations reduce to complex-valued equations with a real parameter, and can be solved by the techniques of ordinary differential equations.

The next step is to trace complex rays to specific receivers (two-point ray tracing). We will restrict our attention to two-dimensional models. Extension to higher dimensions is computationally more expensive, but presents no theoretical difficulties. The goal is to find rays that intersect a particular real receiver $\mathbf{x}_f = (x,z)$. Let θ parametrize the initial wave front; in two dimensions θ contains one complex variable. We seek complex pairs $\mathbf{y} = (\theta,\nu)$ such that $\mathbf{x}(\mathbf{y}) = \mathbf{x}_T$, where $\mathbf{x}$ is the function given in the first line of Eq. (20). The forward problem of computing $\mathbf{x}(\mathbf{y})$ can be solved numerically with an ordinary diffential equation (ODE) solver; the inverse problem can be solved by combining this with a modified Newton's method. This alternating ODE solver-Newton's method approach is well known, and for ν and θ_0 real is widely used in real ray tracing. The complex version was suggested implicitly in [22] and has been implemented for simple models by [25,37], and others.

Explicitly, begin with an initial guess in ray-centered coordinates $\mathbf{y}_1 = (\theta_1,\nu_1)$. Let $\delta\mathbf{y} = (\delta\theta, 0)$, where $\delta\theta$ is a fixed perturbation much smaller than the desired final accuracy in θ. Let $i=1$. First an ODE solver (the authors use fourth-order variable stepsize Runge-Kutta; see [30]) is used to compute

$$\mathbf{x}_i = \mathbf{x}(\mathbf{y}_i) \tag{24}$$

$$\mathbf{x}_i' = \mathbf{x}(\mathbf{y}_i + \delta\mathbf{y}) \tag{25}$$

$$\mathbf{p}_i = \mathbf{p}(\mathbf{y}_i). \tag{26}$$

Then the Jacobian matrix is evaluated at the guess point

$$\mathbf{J}(\mathbf{x}_i) = \left.\left(\frac{\partial \mathbf{x}}{\partial \mathbf{y}}\right)\right|_{\mathbf{x}_i} = \left.\begin{pmatrix} \dfrac{\partial x}{\partial \nu} & \dfrac{\partial x}{\partial \theta} \\ \dfrac{\partial z}{\partial \nu} & \dfrac{\partial z}{\partial \theta} \end{pmatrix}\right|_{(x_i,z_i)} \approx \begin{pmatrix} p_{xi} & \dfrac{x_i' - x_i}{\delta\theta} \\ p_{zi} & \dfrac{z_i' - z_i}{\delta\theta} \end{pmatrix}. \tag{27}$$

The Jacobian is then used to improve the guess using an iteration of Newton's method

$$\mathbf{y}_{i+1} = \mathbf{y}_i + \mathbf{J}(\mathbf{x}_i)^{-1}[\mathbf{x}_T - \mathbf{x}_i]. \tag{28}$$

Then i is incremented and the steps in Eqs. (27) and (28) are repeated. The algorithm is terminated when $\mathbf{x}_i$ comes within some desired precision ϵ of $\mathbf{x}_T$

$$|\mathbf{x}_T - \mathbf{x}_i| < \epsilon \tag{29}$$

and the final estimate $\mathbf{y}_i$ results. If this condition is not met within some desired number of iterations k, a null guess is returned. We will use the notation

$$N_{\epsilon,k}(\mathbf{x}_T,\mathbf{y}_1) \tag{30}$$

to denote the result of this algorithm (whether null or vector), given target $\mathbf{x}_T$, initial guess $\mathbf{y}_0$, and parameters ϵ and k as above.

For more complicated models, difficulties are encountered. Newton's algorithm converges only when the initial guess is sufficiently close to the target receiver. When no initial guess is known, finding rays can be expensive. It is not practical to simply shoot out a "fan" of complex rays: There are two real dimensions of initial conditions θ_0 to choose from in order to select a ray, and then arg ν must be chosen in order to select a path. There are therefore three degrees of freedom in the selection of a path. This contrasts to the single-parameter initial conditions in real ray tracing. In higher dimensions, complex rays compare even more unfavorably: In n dimensions, there are $n-1$ degrees of freedom for real rays and $2n-1$ degrees of freedom for complex paths. Thus, global searches with complex rays are to be avoided when possible.

The purpose of our algorithm will be to find most of the complex rays of interest without recourse to such global searches. In the case of rays in the shadow of one or more caustics, we will find all of the significant complex rays using carefully selected local methods. In particular, a family of rays can be continuously tracked along an array of receivers, once a ray to any one receiver has been found. For each family of rays an initial receiver can usually be chosen so that the ray traced to it is purely real, and thus easy to find. The ray is then tracked along the receiver array as it becomes complex, and no global search is required. Colloquially speaking, we lock on to the rays where they are easy to see and then follow them into uncharted territory.

To make this idea more precise, suppose it is desired to find complex rays from a source to each of a sequence of real receivers $\mathbf{r}_p=(x_p,z_p)$, $p=1,\ldots,N$, with $|\mathbf{r}_{p+1}-\mathbf{r}_p|$ small for $p=1,\ldots,N-1$. Apply the following algorithm:

1. Compute all real rays to each receiver using the standard techniques of real ray-tracing. That is, find the set of solutions $\mathcal{R}_p=\{\mathbf{y}_{p,1},\ldots,\mathbf{y}_{p,n_p}\}$ to the equation $\mathbf{x}(\mathbf{y})=\mathbf{r}_p$. Denote the components of $\mathbf{y}_{p,i}$ by $\mathbf{y}_{p,i}=(\nu_{p,i},\theta_{p,i})$. If there are no real rays at any point, extend the receiver line until at least one real ray is found.

2. The next step is to use the rays hitting each receiver as initial guesses for the next receiver. Pick a suitable ϵ and k. For $i=1,\ldots,n_p$, let

$$\mathbf{y}_{p,i}' = N_{\epsilon,k}(\mathbf{r}_{p+1},\mathbf{y}_{p,i}) \tag{31}$$

and let

$$\mathcal{R}_p' = \{\mathbf{y}_{p,i}' | i \in \{1,\ldots,n_p\}, \mathbf{y}_{p,i}' \neq \varnothing\} \tag{32}$$

3. Now eliminate redundant rays, to ensure counting is done correctly. To do this, define a distance function between two rays

$$d(\mathbf{y}_1,\mathbf{y}_2) = \max\left(\left|J\right|_{\mathbf{y}_1}(\mathbf{y}_1-\mathbf{y}_2)\right|,\left|J\right|_{\mathbf{y}_2}(\mathbf{y}_1-\mathbf{y}_2)\right|\right), \tag{33}$$

where J is the Jacobian matrix in Eq. (27). If there exists a pair of rays $\mathbf{y}_{p,i}',\mathbf{y}_{p,j}' \in \mathcal{R}_p'$ such that

$$d(\mathbf{y}_{p,i}',\mathbf{y}_{p,j}') < \epsilon, \tag{34}$$

then find the larger of $d(\mathbf{y}_{p,i}',\mathbf{y}_{p,i})$ and $d(\mathbf{y}_{p,j}',\mathbf{y}_{p,j})$ and delete from $\mathcal{R}_p'$ the ray to which it corresponds. Continue deleting rays until no pair of rays in $\mathcal{R}_p'$ satisfies Eq. (34).

4. Since complex rays cannot be found by applying Newton's method to real rays, it is necessary to use some type of perturbation technique on the rays that leave the real plane. Let

$$\mathcal{L}_p = \{\mathbf{y}_{p,i} \in \mathcal{R}_p | \mathbf{y}_{p,i}' \notin \mathcal{R}_p'\}. \tag{35}$$

Split $\mathcal{L}_p$ further into complex and strictly real rays

$$\mathcal{L}_p^r = \{\mathbf{y} \in \mathcal{L}_p | \mathbf{y} \in \mathbb{R}^2\} \tag{36}$$

$$\mathcal{L}_p^i = \{\mathbf{y} \in \mathcal{L}_p | \mathbf{y} \notin \mathbb{R}^2\}. \tag{37}$$

Let $\Delta\nu$ and $\Delta\theta$ be parameters, and let

$$\Delta^r = \{(i\Delta\nu, \pm i\Delta\theta),((i+1)\Delta\nu, \pm(i+1)\Delta\theta)\} \tag{38}$$

$$\Delta^i = \{(\pm i\Delta\nu \pm \Delta\nu, \pm i\Delta\theta \pm \Delta\theta)\}, \tag{39}$$

where all ± signs are allowed to vary independently. Let

$$\begin{aligned}\mathcal{R}_p'' = \{&N_{\epsilon,k}(\mathbf{r}_{p+1},\mathbf{a}+\mathbf{y}) | \mathbf{a} \in \Delta^r \quad \text{and} \quad \mathbf{y} \in \mathcal{L}_p^r\} \\ &\cup \{N_{\epsilon,k}(\mathbf{r}_{p+1},\mathbf{a}+\mathbf{y}) | \mathbf{a} \in \Delta^i \quad \text{and} \quad \mathbf{y} \in \mathcal{L}_p^i\}.\end{aligned} \tag{40}$$

Let $\mathcal{R}_p'''=\mathcal{R}_p' \cup \mathcal{R}_p''$, and repeat the procedure in step 3 to remove duplicates from $\mathcal{R}_p'''$.

5. Now add the new rays found in steps 2–4 to the database: For each $\mathbf{y} \in \mathcal{R}_p'''$, if

$$d(\mathbf{y},\tilde{\mathbf{y}}) > \epsilon \tag{41}$$

for every $\tilde{\mathbf{y}} \in \mathcal{R}_{p+1}$, then set $\mathcal{R}_{p+1} = \{\mathbf{y}\} \cup \mathcal{R}_{p+1}$. Update the labeling of the elements of $\mathcal{R}_{p+1}$ appropriately.

6. Repeat steps 2 through 5 for $p=2,3,\ldots,(N-1)$.

7. Repeat steps 2 through 6 working backward from $p=N$ to $p=2$ [with $(p+1)$ replaced everywhere by $(p-1)$]. The purpose of this step is to track real rays that become complex as the receiver line is traversed in the opposite direction.

Step 4 is the crucial step in this algorithm. Because the total number of complex rays (including real rays) reaching a point is constant, but the number of real rays alone is not, it is easy to tell where rays leave the real plane and which rays do so. Searching a cluster of complex guesses (Δ^r) around the ray's last known position then finds it as it departs from real (ν,θ) space. Once found, the complex rays occasionally get lost again; the grid search around Δ^i attempts to recover them. Careful tuning of the parameters $\Delta\nu$ and $\Delta\theta$ greatly improves the probability of finding new rays. These parameters must be large enough to escape the basin of attraction of the known rays, but small enough that the algorithm remains stable. In our implementation, we have determined these parameters by trial and error. A more systematic approach would likely have improved the algorithm's performance.

The above algorithm has some limitations. First, rays are increasingly likely to be lost as they are tracked farther into the shadow zone. In some models, these "deeply complex" rays can be significant. However, such models usually involve strong discontinuities or chaotic complex rays; see, for example, [38]. In smooth models with no chaos on the relevant scales, wave fields in the deep shadow zone are usually very small. In particular, these rays may be neglected in the typical smooth seismic velocity model.

Second, the algorithm fails to detect rays that are everywhere nonreal along the receiver line. These rays can be divided into three types: (i) those from the shadow zone of a real caustic which passes close to, but does not cross, the receiver line; (ii) those from the shadow zone of a distant real caustic; and (iii) those from the shadow zone of a caustic in complex space. Type (i) rays can be found by extending the receiver line to cross the caustic in question. Type (ii) rays can usually be ignored, as discussed above. Type (iii) rays are potentially significant if a complex caustic passes close to real space without intersecting. These rays could be found by doing a grid search around every real receiver instead of just those where a real ray departs; such a search would, however, increase computational cost.

Third, the procedure may not work correctly if the segment between two adjacent receivers crosses more than one caustic. In this case some rays may rejoin the real plane while an equal number depart, so that both events go undetected. This can be remedied by increasing the density of receivers in areas with multiple caustics. Fourth, the procedure fails entirely if a receiver lies exactly on a caustic and works more slowly in the vicinity of caustics. This is an issue with Newton's method rather than with the tracking algorithm itself; the Jacobian matrix $\mathbf{J}$ is singular at a caustic and so Eq. (28) is ill-defined there. Generically, receivers will not fall exactly on caustics, but the increased computational cost near caustics cannot be avoided.

Quantities of Motion

The travel time T is straightforward and can be computed from Eq. (21) once the ray path is known. The ray spreading follows from the Jacobian matrix, which has already been calculated as part of the ray-finding algorithm. The amplitude A can be determined up to a sign from Eq. (23), but the value of that sign must be determined according to the prescriptions in Sec. III. Choose an initial branch for the amplitude on one ray. Away from caustics, the branch can be traced continuously as J changes from receiver to receiver. At a caustic, where (generically) two real rays become two complex rays, the sign of A on any of the four rays determines the sign on the other three, depending on T and J as in Sec. III. In this way, choices of the amplitude branch can be linked over all rays on all receivers.

V. MODEL REPRESENTATION

Given formulas for the quantities of motion, the goal is now to calculate them for realistic velocity models. In order to do this, we must address the issue of model representation.

The inverse square of the velocity model, $s^2(x,z) = c^{-2}(x,z)$, must be analytic for the complexified Hamilton's equations to make sense. This requirement raises the issue of model representation. The usual approach in real ray tracing is to perform a bilinear or cubic spline interpolation on the given discrete velocity model. However, the higher-order discontinuities at the interfaces of the interpolation cells become zeroth-order (jump) discontinuities when analytically continued into the complex plane, due to the inherently unstable nature of analytic continuation. Local interpolation therefore cannot produce even a continuous model.

Two strategies are available for circumventing this obstacle. The first is to accept these discontinuities and treat them as interfaces. This approach allows model representation to remain local, but also has significant drawbacks. Large numbers of interfaces complicate the algorithm for ray tracking and slow its convergence. Furthermore, the regularity of these interfaces may introduce artifacts in the ray paths themselves.

The second strategy is to fit all the data to a global analytic function, thereby avoiding all discontinuities and artificial interfaces. The key drawback is the computational cost of evaluating the fitting function (which potentially has an enormous number of terms) at every point along every ray path. Obviously, one can imagine hybrid strategies in which separate fitting functions are applied to each of a small number of "regions" of the velocity model, and interfaces are formed between neighboring regions. The size of the regions can then be chosen to produce an acceptable trade off between interface errors and evaluation costs. Because interfaces are not the focus of this paper, we have chosen to use a global fitting function. It is emphasized, however, that there is no theoretical or practical impediment to the other approaches.

Two-dimensional polynomials might seem to be the obvious fitting functions. Unfortunately, high-order polynomials tend to exhibit erratic behavior both between the fitting points and at even small distances away from the real plane.

Polynomial fitting is also unstable and numerically problematic. A better method is to apply a 2D discrete cosine transform (DCT) to the velocity model and use the resulting expansion as the fitting function.

Explicitly, let $s^2(x_i,z_j)$ be a uniformly spaced rectangular grid of inverse-square velocity values, where $i=0,1,\ldots,(n_x-1)$, $j=0,1,\ldots,(n_z-1)$. Apply the transformation

$$q_{i,j} = \frac{2}{\sqrt{n_x n_z}} a_i a_j \sum_{k=0}^{n_x-1} \sum_{l=0}^{n_z-1} s^2(x_k,z_l) \cos\left[\frac{k\pi}{2n_x}(2i+1)\right] \times \cos\left[\frac{l\pi}{2n_z}(2j+1)\right], \qquad (42)$$

where $a_i=1$ for $i>1$ and $a_1=1/\sqrt{2}$. Then let

$$f(x,z) = \frac{2}{\sqrt{n_x n_z}} \sum_{k=0}^{n_x-1} \sum_{l=0}^{n_z-1} a_k a_l q_{k,\ell} \cos\left[\frac{k\pi}{2n_x}\left(\frac{2(x-x_0)}{\Delta_x}+1\right)\right] \times \cos\left[\frac{l\pi}{2n_z}\left(\frac{2(z-z_0)}{\Delta_z}+1\right)\right], \qquad (43)$$

where $\Delta_x = x_1 - x_0$ and $\Delta_z = z_1 - z_0$ are the spacings between grid rows and columns. The function $f(x,z)$ is analytic everywhere, real in the real plane, and has the property $f(x_i,z_j)=s^2(x_i,z_j)$.

In theory the evaluation of f requires $O(n_x n_z)$ steps, but for typical models many of the higher wave-number coefficients $q_{i,j}$ are negligible. If evaluation time still presents a problem, f and its derivatives can be tabulated at four-dimensional lattice points and the appropriate local approximations can be used.

The function f is essentially a sum of exponentials far from the real plane, and will increase rapidly at large distances from that plane. That is, the fit will be well-behaved in a region whose projection on the imaginary x-imaginary z plane is a finite region about the origin. The radius of this region is of the order of the characteristic scale of variation of the original model data.

Figure 2(a) shows a velocity model from the Yucca Mountain (Nevada), obtained using crosswell tomography. Yucca Mountain is a potential repository for nuclear waste. Its subsurface structure has been studied extensively using various geophysical, geochemical, and hydrological techniques (for more information see http://ocrwm.doe.gov/osti/index.shtml). One of the geophysical surveys done was a crosswell survey by Lawrence Berkeley National Laboratory (Berkeley, CA). By applying travel time tomography on this data set the velocity model shown in Fig. 2(a) was derived. This model shows quite significant velocity variations (up to 20%). Ray paths computed using this model give rise to caustics and therefore multipathing (as is clear from Fig. 2 for a particular source).

Superimposed upon the Yucca model is a fan of real rays from a point source traced using the usual cubic spline interpolation. Figure 2(b) shows the same model, with rays traced using the DCT expansion. The two sets of rays are nearly indistinguishable. Figures 3(a) and 3(b) show cross sections of the absolute value of the model in the $\mathrm{Im}(x)-\mathrm{Re}(z)$ plane and the $\mathrm{Re}(x)-\mathrm{Im}(z)$ planes. The characteristic length scale appears to be $1-1.5$ m in both dimensions; within this region the velocity is well-behaved. Outside the region, $|c|\to 0$, as expected from $|c^{-2}|=|s^2|\to\infty$. Plots of the phase of c, shown in Figs. 3(c) and 3(d), confirm this behavior; the phase is stable and approximately zero over the same $1-1.5$ m region.

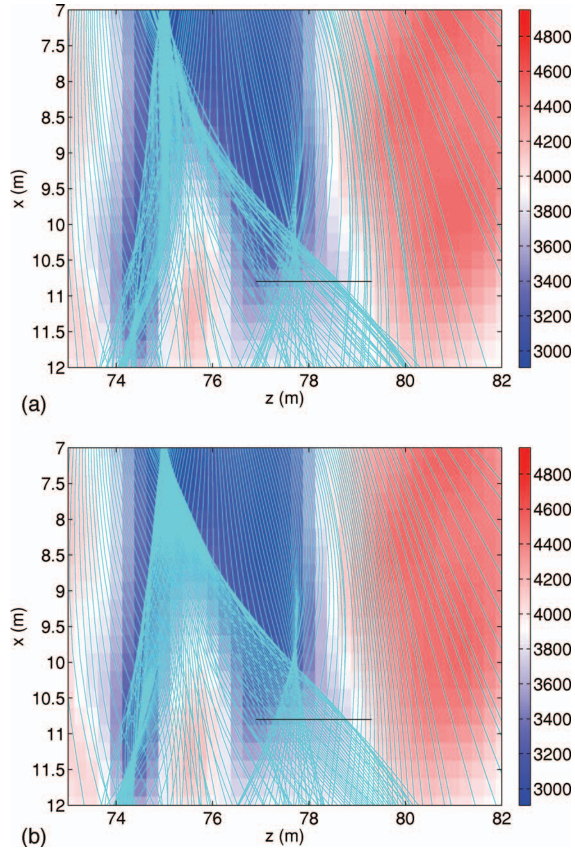

FIG. 2. (Color) (a) Propagation velocity derived from Yucca Mountain crosswell data, cubic spline interpolated from square grid with spacings 0.5 m. Superimposed is a fan of rays shot from a point source at (75,2). (b) Same data with rays computed from DCT fitting. The two ray fans are visually distinguishable only in a small (0.15 m) apparent offset of the DCT rays toward the right. The black line is the receiver array. All colorbars measure velocity in m/s.

VI. IMPLEMENTATION OF RAY-TRACING ALGORITHM

This section applies our complex ray tracing algorithm of Sec. IV to the DCT fitted models of the last section.

A. Test Model

We first test our algorithm on a well-known analytic model with an analytic solution, the point source in a linear layer. The solution of this problem can be found in [39] and [22]. We take as our velocity model $c^{-2}(x,z)=z^{-1/2}$, with the point source at $x=1, z=1$. The initial value surface is parametrized by a complex takeoff angle θ; the ray trajectories are

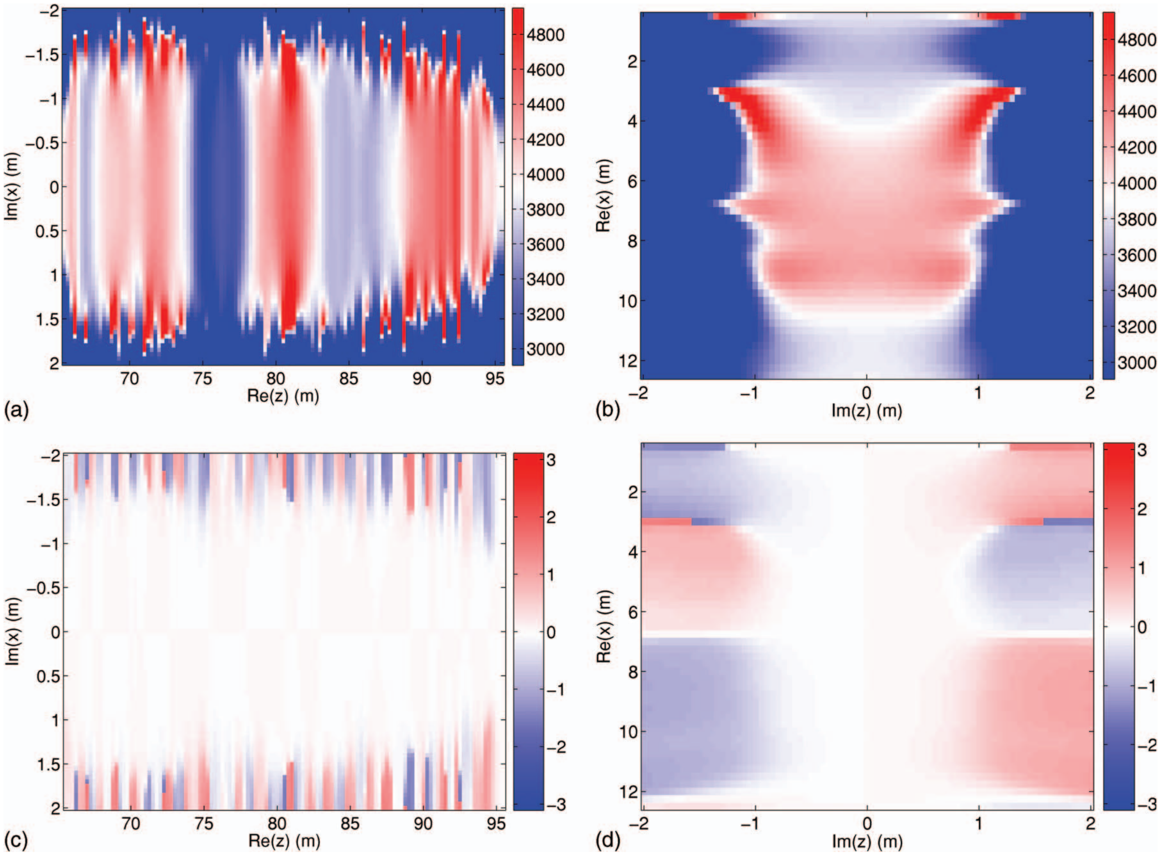

FIG. 3. (Color) Cross sections of the DCT fitting function amplitude at (a) Re(x)=7, Im(z)=0 and at (b) Im(x)=0, Re(z)=79. (c) Cross section of the fitting function phase for the same region as (a). (d) Cross section of the fitting function phase for the same region as (b). Sharp phase and amplitude instability occur beyond $x=1$ m and $z=1.5$ m outside the real plane. Note that velocity c is graphed, but c^{-2} was fit to the DCT. The colorbars of (a) and (b) give velocity in m/s; the colorbars of (c) and (d) are in radians.

$$x = \nu \cos \theta + 1$$

$$z = \nu \sin \theta + \frac{1}{4}\nu^2 + 1. \qquad (44)$$

The travel time and Jacobian functions are

$$T(x,z) = \frac{2}{3}(z + 1 - 2w_c^{1/2})^{1/2}[z + 1 + w_c^{1/2}] \qquad (45)$$

$$J(x,z) = 2w_c^{1/2}(z + 1 - 2w_c^{1/2})^{1/2}, \qquad (46)$$

where $w_c = z-(x-1)^2/4$. There is one fold caustic, which has the equation $w_c=0$. Two rays arrive at every point in the real plane; on one side of the caustic they are both real and on the other side both are complex. The results of the numerical simulation agree with these predictions and with Eqs. (45) and (46). The numerically traced real and complex rays, projected onto real space, are shown superimposed upon the model in Fig. 4(a). The same rays are shown in the three dimensions $(\mathrm{Re}\,x, \mathrm{Re}\,z, \mathrm{Im}\,z)$ from various viewpoints in Figs. 4(b) and 4(c), and 4(d). Note how the two families of real rays coalesce and then escape vertically from the real plane.

Motion in the $\mathrm{Im}\,x$ plane is trivial for this model, hence the 3D graphs are not projections but full representations of the ray paths. This reduced dimensionality is a consequence of lateral symmetry and does not hold for general velocity functions.

B. Yucca Mountain Model

The algorithm is next applied to the Yucca mountain velocity model, using the DCT model representation in Sec. V. Real ray tracing reveals that rays shot from a point source at $z=75$, $x=2$ produce several cusp caustics. The receiver line, placed along $x=11$ has one, three, and five real arrivals at various places. The results of the ray tracing are shown in Fig. 5. Five rays are found almost everywhere along the receiver line, including in the shadow zones of both caustics. Rays are found leaving the real plane in three separate places along the receiver line, including both right-to-left and left-to-right departures. At the far end of the receiver spread, two complex rays are lost, corresponding to the deep shadow zone of the inner caustic. The wave forms in Sec. VIII will show that the contributions of these rays were very small. The rays are lost due to the failure of Newton's method in unstable regions of the velocity model. This instability can be seen in Fig. 5(b), where the last traceable complex rays exhibit abrupt curvature at a distance 1 m away from the real plane. As expected, this curvature occurs near the edge of the region of stability identified in Sec. V.

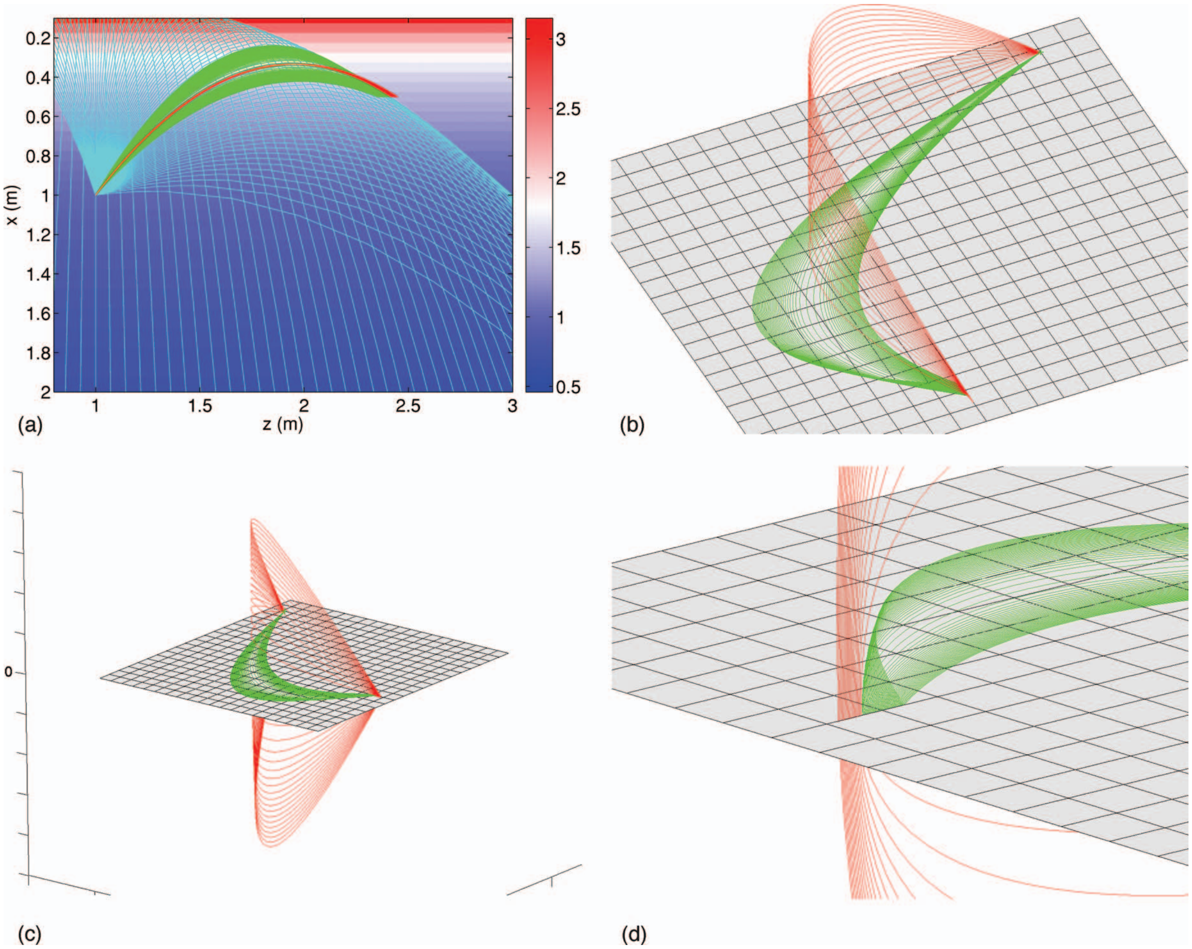

FIG. 4. (Color) Complex ray tracing in the linear layer from a point source at (1,1). (a) A fan of rays superimposed on the model (blue), with tracing of selected real (green) and nonreal (red) rays. Colorbar measures velocity in m/s. (b), (c), (d) 3D projections of the complex paths in various views. The gray tiled surface is the plane Im(x) = Im(z) = 0; the third axis is $\sqrt{\mathrm{Im}(z)^2+\mathrm{Im}(x)^2}$. The coalescing of two families of real rays and their escape into the complex plane can be seen most clearly in (c).

VII. PHASE FUNCTION COMPUTATION

Now that the missing travel times and amplitudes from Sec. II are accessible, Eqs. (14)–(18) can at last be solved. The amplitude Eqs. (16) and (18) can be solved by a linear transformation, but the equations for the phase polynomial are nonlinear. It is necessary to solve

$$\frac{1}{N+1}\theta_i^{N+1}+\sum_{n=0}^{N-1}P_n\theta_i^n=T_i \quad i=1,\ldots,N \tag{47}$$

$$\theta_i^N+\sum_{n=1}^{N-1}nP_n\theta_i^{n-1}=0 \quad i=1,\ldots,N \tag{48}$$

for the $2N$ variables P_n and θ_n at a fixed point $\mathbf{x}$. If we specify that the phase function must be real, then there is a unique solution. Note that we are allowed to transform the independent variable and write the polynomial in terms of the transformed variable. Thus, we seek both the transformed roots of the polynomial and the coefficients of the polynomial, rendering the problem nonlinear. We adopt an iterative perturbation approach in which we perturb the coefficients of the polynomial.

Explicitly, the convergence algorithm consists of two alternating steps. First, given an estimate $\hat{P}_n$, $n=0,\ldots,N-1$, of the coefficients in Eqs. (47) and (48), we find the roots of Eq. (48), labeling them θ_i, $i=1,\ldots,N$. Then Eqs. (47) may be rewritten as

$$\sum_{n=0}^{N-1}(\delta P)_n\theta_i^n=T_i-\sum_{n=0}^{N-1}\hat{P}_n\theta_i^n-\frac{1}{N+1}\theta_i^{N+1}, \tag{49}$$

with $(\delta P)_n=P_n-\hat{P}_n$, or equivalently as

$$\mathbf{A}\mathbf{x}=\mathbf{b}, \tag{50}$$

where

$$A_{ij}=\begin{cases}\mathrm{Re}\ \theta_i^{j-1}, & 1\leqslant i,j\leqslant N;\\ \mathrm{Im}\ \theta_{i-N}^{j-1}, & N<i\leqslant 2N, 1\leqslant j\leqslant N\end{cases} \tag{51}$$

and

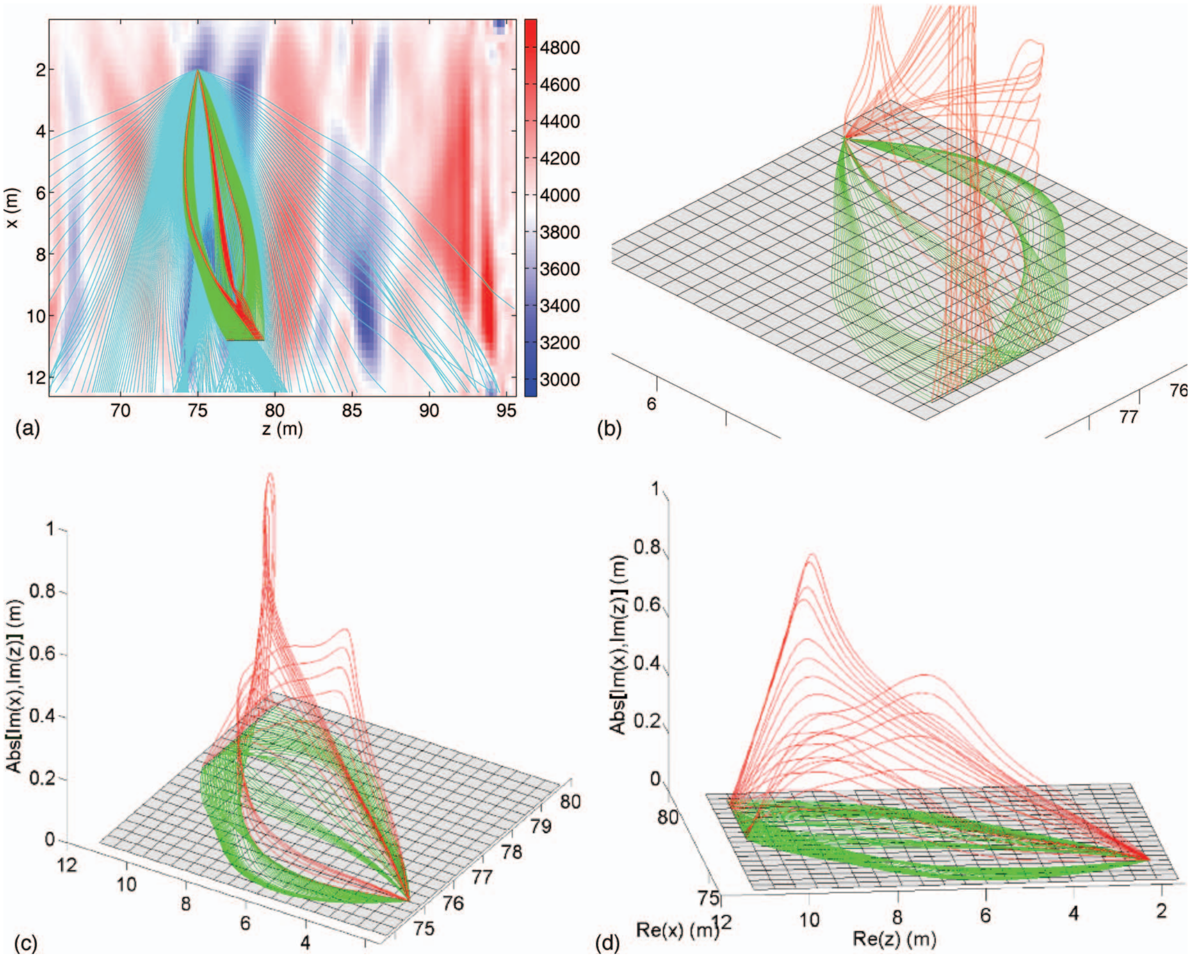

FIG. 5. (Color) Complex ray tracing in the Yucca Mountain model from a point source at (75,2). (a) A fan of rays superimposed on the model (blue), with tracing of selected real (green) and nonreal (red) rays. (b), (c), (d) 3D projections of the complex paths in various views. The gray tiled surface is the plane Im(x) = Im(z) = 0; the third axis is $\sqrt{\mathrm{Im}(z)^2+\mathrm{Im}(x)^2}$. Coalescing of real rays can be seen in (b). A combination of (b), (c), and (d) shows the sharp curvature of the complex rays far from the real plane. The colorbar gives velocity in m/s.

$$b_i = \begin{cases} \mathrm{Re}\left(T_i - \sum_{n=0}^{N-1} \hat{P}_n \theta_i^n - \frac{1}{N+1}\theta_i^{N+1} \right), & i \leqslant N; \\ \mathrm{Im}\left(T_{i-N} - \sum_{n=0}^{N-1} \hat{P}_n \theta_{i-N}^n - \frac{1}{N+1}\theta_{i-N}^{N+1} \right), & N < i \leqslant 2N \end{cases} \tag{52}$$

and $x_j=(\delta P)_{j-1}$, $1 \leqslant j \leqslant N$. Equation (50) is then solved for $\mathbf{x}$ using a singular value decomposition with norm regularization [40]. The perturbations $(\delta P)_n$ are then used to form a new estimate of the polynomial coefficients, and the process is repeated. Our algorithm is similar to, yet simpler than, the one proposed by Connor and Curtis [27] as part of a procedure for approximating oscillating integrals. In particular, the singular value decomposition allows the algorithm to remain stable near caustics, where the matrix $\mathbf{A}$ is ill conditioned.

The initial guess for the polynomial coefficients is estimated by a combination of two methods. For the first receiver in the line, we generate initial coefficients using symmetric functions ([41], p. 318), based upon the initial takeoff angles of the rays associated with the given arrival times. For subsequent receivers, we use the polynomial computed for the previous receiver as an initial guess. In theory the algorithm should work for any number of arrivals. In practice, there sometimes exist stable fixed points which do not actually solve the polynomial equations. Whenever one of these "pseudosolutions" is encountered, we apply a random perturbation and repeat the iteration. We find that the algorithm is stable and converges to a genuine solution within a few tens of iterations. We have tested it for up to five arrivals (both real and complex), the maximum number produced by our velocity models.

As a final point, note that the arrivals from all complex rays have been used in our construction of phase polynomials, including the "unphysical" rays. Selection rules and Stokes' phenomenon thus play no role in the construction of phase functions.

VIII. TIME DOMAIN WAVE FIELD

By combining the two algorithms presented in Secs. IV and VII, time-domain wave forms for both geometric and uniform asympotics can be computed for both real and complex rays. Consider the time-domain Helmholtz equation with analytic source wavelet $s(t)$

$$\nabla^2 v - \frac{1}{c(\mathbf{x})^2}\frac{\partial^2 v}{\partial t^2} = (s(t) + i\mathbb{H}s(t))\delta^3(\mathbf{x}). \tag{53}$$

The real part of v is the desired wave field. Using the geometric ray ansatz, Eq. (7), at each frequency and transforming the result into the time domain gives the resultant wave field

$$u(\mathbf{x},t) = \mathrm{Re}\, v(\mathbf{x},t) = \sum_{n=1}^{N} \mathrm{Re}[A_n(\mathbf{x})s(t - T_n(\mathbf{x})) + iA_n(\mathbf{x})\mathbb{H}s(t - T_n(\mathbf{x}))], \tag{54}$$

as derived in [42]. We take as our source wavelet the boxcar function

$$B_\delta(t) = \begin{cases} \dfrac{1}{2\delta}, & \text{if } t \in \mathbb{R} \text{ and } -\delta < t < \delta; \\ 0, & \text{otherwise.} \end{cases} \tag{55}$$

For real t the Hilbert transform of $B(t)$ is

$$\mathbb{H}B_\delta(t) = \frac{1}{2\pi\delta}\int_{-\delta}^{\delta}\frac{d\xi}{\xi - t} = \frac{1}{2\pi\delta}\ln\left(\frac{|\delta - t|}{|\delta + t|}\right), \tag{56}$$

and for nonreal t it is

$$\mathbb{H}B_\delta(t) = \frac{1}{2\pi\delta}\left[\ln\left(\frac{|\delta - t|}{|\delta + t|}\right) + i[\arg(\delta - t) - \arg(-\delta - t)]\right], \tag{57}$$

where arg denotes the standard branch of the argument, $-\pi < \arg(z) \leq \pi$. Substitution of Eqs. (55), (56) and (57) into Eq. (54) yields

$$u(\mathbf{x},t) = \frac{1}{2\pi\delta}\sum_{n=1}^{N}\Bigg[\mathrm{Re}(A_n(\mathbf{x}))[\arg(\delta - t + T_n(\mathbf{x})) - \arg(-\delta - t + T_n(\mathbf{x}))] - \mathrm{Im}(A_n(\mathbf{x}))\ln\left(\frac{|\delta - t + T_n(\mathbf{x})|}{|\delta + t - T_n(\mathbf{x})|}\right)\Bigg]. \tag{58}$$

Note that the real and complex cases yield different Hilbert transforms, but the final wave field is the same because $B_\delta(t) = 1/(2\pi\delta)[\arg(\delta - t) - \arg(-\delta - t)]$ for real t.

We now want a similar formula for wave forms from the integral representations derived in Sec. I. One option is to take advantage of the fact that the phase and amplitude functions have been chosen so that the integral representation is a linear combination of a generalized Airy function

$$A(p_1, p_2, \ldots, p_{N-1}) = \int_{-\infty}^{\infty}\exp\left[i\left(\frac{1}{N+1}\theta^{N+1} + p_{N-1}\theta^{N-1} + p_{N-2}\theta^{N-2} + \cdots + p_1\theta\right)\right]d\theta \tag{59}$$

and its derivatives. Fast algorithms for evaluating the standard integrals and their derivatives have been developed for both the frequency domain (see [28] and more recently [43]) and the time domain [34]. However, these methods work best when the number of parameters in the integral is small; for $N > 4$ they become more involved. In fact, only the cases $N \leq 4$ have been tried numerically in the above references. Normally this would not be a problem in two dimensions, where $N \leq 3$ because only the simple caustic and cusp caustic occur. However, because the phase functions in Sec. VII can encompass several caustics in a global continuous solution, $N > 3$ may occur even in two dimensions. For example, $N = 5$ was required in the Yucca Mountain velocity model.

For this reason, standard integrals will be avoided in favor of more direct evaluation. A formula analogous to Eq. (58) can be derived by using Eq. (8) instead of Eq. (7) as the frequency-domain ansatz. As derived in [44], it is

$$u(\mathbf{x},t) = 2^{-1/2}\pi^{-1}\frac{d}{dt}\left[\frac{H(t)}{t^{\frac{1}{2}}} * \int_{-\infty}^{\infty}\mathrm{Re}(a(\mathbf{x},\theta))B_\delta(t - \Phi(\mathbf{x},\theta))d\theta - \frac{H(-t)}{(-t)^{\frac{1}{2}}} * \int_{-\infty}^{\infty}\mathrm{Im}(a(\mathbf{x},\theta))B_\delta(t - \Phi(\mathbf{x},\theta))d\theta\right], \tag{60}$$

where H is the Heaviside step function. For each t, the integrals in Eq. (60) are nonzero only where $|t - \Phi(\mathbf{x},\theta)| < \delta$, which consists of a small number of thin bands. The evaluation time of the wave field per value of $\mathbf{x}$ and t is therefore of order unity, provided that the evaluations are done at a sampling interval of at least δ. We use the algorithm presented in [45], which was provided to the authors by C. Chapman. This algorithm samples a and Φ at spacing δ and uses linear interpolation to sum the integrals in Eq. (58). The linear approximation does not incur significant error because the resulting wave form is already bandlimited by the boxcar width δ.

Figure 6 shows wave forms for the linear velocity model. Figure 6(a) is a wave form from only real geometric arrivals. Figure 6(b) incorporates complex geometric arrivals. Because only a simple caustic is present in the linear layer, the inclusion of complex rays has the sole effect of introducing a decaying wave field in the shadow zone. Note the unphysically rapid growth of the wave field on either side of the caustic in Fig. 6(b). Figure 6(c) shows uniform asymptotics derived from real arrivals only. Near the caustic, the wave field no longer blows up. Finally, Fig. 6(d) shows uniform asymptotics derived from real and complex arrivals. These complex uniform wave forms combine the advantages of complex geometric and real uniform wave forms; the wave field is smooth near the caustic and exists in the caustic shadow. It is Fig. 6(d) that most closely resembles the analytical airy integral solution of the linear layer.

Far away from the caustic, geometric ray tracing is accurate, so the wave field in Fig. 6(d) should be identical to that of Fig. 6(b) except near the caustic. In our simulation, the peaks do occur in the same place, but the peaks from uniform asymptotics (Fig. 6(d)) are broader and shorter than the peaks from geometric asymptotics (Fig. 6(b)). Areas are however preserved under this distortion. This effect is also visible in Fig. 13 of [42] and may be attributed to differences

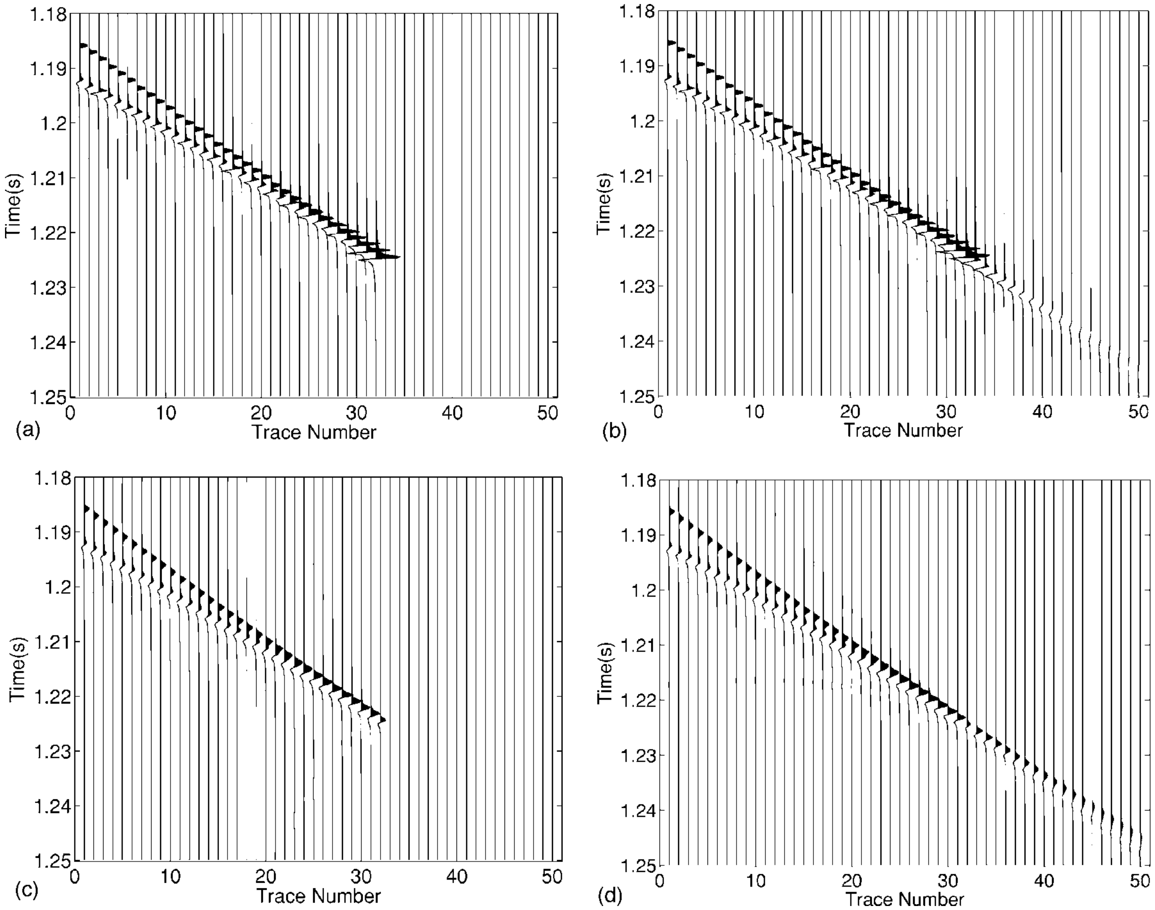

FIG. 6. Wave forms from the linear layer model of Fig. 4(a), near a fold caustic. Traces run from (2.35,0.5) to (2.45,0.5) in increments of (0.002,0). (a) Real geometric arrivals only. (b) Complex geometric arrivals. Note the addition of a decaying wave in the shadow zone. (c) Uniform asymptotics derived from real rays only. Note the smoother behavior near caustics compared to (a) and (b), and the absence of any wave field in the shadow zone. (d) Uniform asympotics derived from complex rays. This last method simultaneously achieves smoothness near caustics and a decaying wave in the caustic shadow. All four subfigures are on the same scale.

in the asymptotic properties of Eqs. (58) and (60). These differences will be negligible after convolution with a broadband Ricker wavelet.

Figure 7 shows wave forms for the Yucca Mountain model, arranged in the same scheme as for the linear velocity model. Here there are five arrivals; within the range of the receiver line they separate out into a cusp and a fold (Fig. 7(a)). If the receiver line were extended to the left, the two structures would meet, forming a cusp inside a cusp. The inclusion of complex rays introduces exponentially decaying wave fields in the shadow zone of the fold and the shadow zones on both sides of the cusp (Fig. 7(b)). Figure 7(c) shows uniform asymptotics for real arrivals only. Far away from the caustics, the integrated peak areas are similar to those of Figs. 7(a) and 7(b), while close to the caustics they are smaller, as expected. Figure 7(d) extends the uniform asymptotics to the complex case, thereby combining the advantages of Figs. 7(b) and 7(c). In each of the three shadow zones (left of cusp, right of cusp, right of fold) there is a smoothly decaying wave field. The decaying wave field left of the cusp is of particular interest, as it introduces an interaction between the fold and the cusp.

It is emphasized that the wave forms of Fig. 7(d) are not equivalent to those that would be obtained by using standard integrals for the cusp and fold separately. Rather, our method roughly amounts to treating the five arrivals as if they were a two dimensional cross section of a butterfly (A_5) caustic [16]. On this particular receiver line the differences would occur chiefly in the area of interaction between the cusp and fold (traces 1–6). In particular, considering all five arrivals together results in a smoother wave field in that area. If the receiver line were extended so as to include the joining of the cusp and fold in a second cusp, further differences might emerge.

IX. DISCUSSION AND CONCLUSIONS

We have presented an algorithm to compute uniformly asymptotic wave forms in the presence of caustics. The algorithm takes the uniformly valid presentation of Ludwig [19], using Eqs. (8) and (11)–(13) as a starting point. We show that the use of complex rays for the computation of the uniform wave forms is necessary. The amplitudes are (asymptotically) correct at and near the caustics (including the shadow zones). The algorithm avoids the “patchwork” problem encountered in practical implementations of Maslov theory and the free parameter present in coherent states and Gaussian beams.

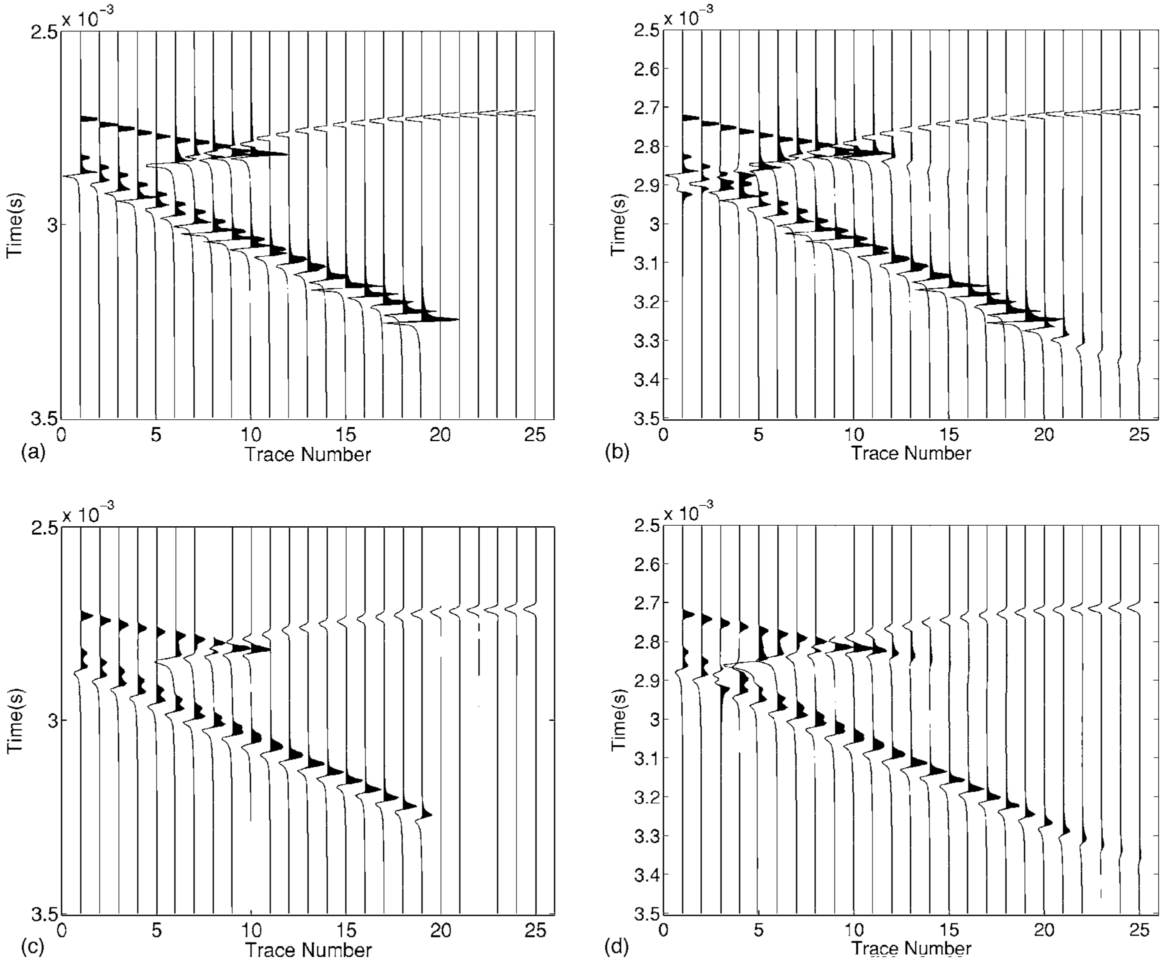

FIG. 7. Wave forms from the Yucca Mountain model of Fig. 5(a). Traces run from (76.8,10.8) to (79.1,10.8) in increments of (0.1,0). (a) Real geometric arrivals only. Note the separation between wavefield triplication in upper part of the wave form and duplication in the lower part. (b) Complex geometric arrivals. Decaying waves show up in the two shadow zones of the triplicated area and one shadow zone of the duplicated area. Note that the duplicated and triplicated areas now interfere. (c) Uniform asymptotics derived from real rays only. (d) Uniform asympotics derived from complex rays. All four subfigures are on the same scale.

The complex ray tracing is done by using an efficient complex two-point ray tracing algorithm. A tracking method is presented for this purpose which greatly reduces the computational cost required in tracing complex rays. The use of a discrete cosine transformation to represent the velocity model makes it possible to compute ray paths in smooth complex valued velocity models. This requires more memory, but makes it possible to avoid the problem of artificial interfaces introduced by local spline representations of the model. A perturbation method was used to compute the polynomial phase function. This enables the computation of wave forms if there are many (more than 3) arrivals.

The algorithm was applied to two models: a simple test model and a velocity model obtained using travel time tomography. The algorithm may be applied to any velocity model (with applications in acoustics, seismology, and electromagnetic wave propagation) or potential function (with applications in semiclassical mechanics).

The results presented are valid for 2D acoustic velocity models. Results could be extended in various directions. The algorithm is also valid in 3D, except near hyperbolic and elliptic umbilic caustics, where single-dimensional integral representations break down. The complex ray tracing could also be used to compute uniform wave forms in anisotropic as well as generally anelastic/poroelastic models. These are topics of ongoing research.

ACKNOWLEDGMENTS

We thank Colin Thomson for several constructive discussions on complex ray tracing. Thanks also to Chris Chapman for providing us with his CCSQRT and THETAC subroutines (Ref. [42]). Most of this research was carried out when D.A. was visiting Schlumberger Cambridge Research. We thank Schlumberger for providing financial support. D. W. Vasco would like to acknowledge the support ot he Assistant Secretary, Office of Basic Energy Sciences of the U.S. Department of Energy under contract DE-AC03–76SF00098.

[1] J. B. Keller and J. S. Papadakis, *Wave Propagation and Underwater Acoustics* (Springer-Verlag, Berlin, 1977).

[2] D. S. Jones, *Acoustic and Electromagnetic Waves* (Oxford University Press, Oxford, 1986).

[3] K. Budden, *Radio Waves in the Ionosphere* (Cambridge University Press, Cambridge, U.K., 1961).

[4] M. Kline and I. Kay, *Electromagnetic Theory and Geometrical Optics* (Interscience, New York, NY, 1965).

[5] K. Budden, *The Propagation of Radio Waves* (Cambridge University Press, Cambridge, U.K., 1985).

[6] V. Cerveny, *Seismic Ray Theory* (Cambridge University Press, Cambridge, U.K., 2001).

[7] C. Chapman, *Fundamentals of Seismic Wave Propagation* (Cambridge University Press, Cambridge, U.K., 2004).

[8] M. C. Gutzwiller, *Chaos in Classical and Quantum Mechanics* (Springer-Verlag, Berlin, 1991).

[9] A. M. O. de Almeida, *Hamiltonian Systems: Chaos and Quantization* (Cambridge University Press, Cambridge, U.K., 1992).

[10] J. E. P. Schneider and E. E. Falco, *Gravitational Lenses* (Springer Verlag, Berlin, 1992).

[11] V. Maslov and M. Fedoriuk, *Semiclassical Approximation in Quantum Mechanics* (Reidel Publications Co., Dordrecht, Holland, 1981).

[12] V. Babich, N. Buldyrev, and I. Molotkov, *Space-Time Ray Method. Linear and Non-Linear Waves* (Leningrad University Press, Leningrad, 1985).

[13] V. Červený, M. Popov, and I. Pšenčik, Geophys. J. R. Astron. Soc. **70**, 109 (1982).

[14] J. Klauder, Ann. Phys. (N.Y.) **180**, 108 (1987).

[15] J. Duistermaat, Commun. Pure Appl. Math. **XXVII**, 207 (1974).

[16] Y. A. Kravtsov and Y. I. Orlov, *Caustics, Catastrophes, and Wave Fields*, 2nd ed. (Springer-Verlag, Berlin, 1998).

[17] C. Chapman and R. Drummond, Bull. Seismol. Soc. Am. **72**, S277 (1982).

[18] J. Kendall and C. J. Thomson, Geophys. J. Int. **113**, 186 (1993).

[19] D. Ludwig, Commun. Pure Appl. Math. **XIX**, 215 (1966).

[20] S. Goldin and A. Duchkov, Stud. Geophys. Geod. **47**, 521 (2003).

[21] B. Seckler and J. Keller, J. Acoust. Soc. Am. **31**, 192 (1959).

[22] C. Thomson, Stud. Geophys. Geod. **41**, 345 (1997).

[23] Y. A. Kravtsov, G. Forbes, and A. Asatryan, in *Progress In Optics*, edited by E. Wolf (Elsevier, Amsterdam, 1999), Vol. XXXIX, pp. 1–62.

[24] S. Chapman, J. Lawry, J. Ockendon, and R. Tew, SIAM Rev. **41**, 417 (1999).

[25] R. A. Egorchenkov and Y. A. Kravtsov, J. Opt. Soc. Am. A **18**, 650 (2001).

[26] Y. A. Kravtsov and P. Berczynski, Wave Motion **40**, 23 (2004).

[27] J. Connor and P. Curtis, J. Math. Phys. **25**, 2895 (1984).

[28] J. Connor, P. Curtis, and D. Farrelly, Mol. Phys. **48**, 1305 (1983).

[29] J. Connor, P. Curtis, and D. Farrelly, J. Phys. A **17**, 283 (1984).

[30] W. H. Press, S. A. Teukolsky, W. T. Vetterling, and B. P. Flannery, *Numerical Recipes in C*, 2nd ed. (Cambridge University Press, Cambridge, 1988).

[31] V. Guillemin and S. Sternberg, *Geometric Asymptotics* (American Mathematical Society, Providence, RI, 1977).

[32] Y. A. Kravtsov, Sov. Phys. Acoust. **14**, 1 (1968).

[33] A. Duchkov, *EAGE 66th Conference and Exhibition* (EAGE, Paris, France, 2004).

[34] A. Hanyga and M. Seredynska, Wave Motion **14**, 101 (1991).

[35] V. Arnol'd, Funct. Anal. Appl. **6**, 61 (1972).

[36] A. Hanyga and H. B. Helle, Geophys. Prospect. **43**, 51 (1995).

[37] T. Van Voorhis and E. J. Heller, Phys. Rev. A **66**, 050501(R) (2002).

[38] T. Onishi, A. Shudo, K. S. Ikeda, and K. Takahashi, Phys. Rev. E **64**, 025201(R) (2001).

[39] Y. A. Kravtsov, Radiophys. Quantum Electron. **10**, 719 (1967).

[40] W. Menke, *Geophysical Data Analysis: Discrete Inverse Theory* (Academic Press, New York, 1989).

[41] D. Cox, J. Little, and D. O'Shea, *Ideals, Varieties, and Algorithms* (Springer-Verlag, New York, NY, 1997).

[42] C. Chapman, J.-Y. Chu, and D. Lyness, in *Seismological Algorithms*, edited by D. Doornbos (Academic Press, New York, 1988), pp. 47–74.

[43] N. Kirk, J. Connor, and C. Hobbs, Comput. Phys. Commun. **132**, 142 (2000).

[44] C. H. Chapman and H. Keers, Stud. Geophys. Geod. **46**, 615 (2002).

[45] C. Chapman, Geophys. J. R. Astron. Soc. **54**, 481 (1978).